Acta Astronautica 202 (2023) 485–496

Contents lists available at ScienceDirect

Acta Astronautica

journal homepage: www.elsevier.com/locate/actaastro

Extreme low-temperature freezing process and characteristic curve of icy lunar regolith simulant

Junwei Liu [a], Weiwei Zhang [a], Jianglei Cui [a], Zhifeng Ren [b], Enliang Wang [b], Xiongyao Li [c], Guangfei Wei [c], Ye Tian [d], Jie Ji [e], Jinan Ma [e], Shengyuan Jiang [a,*]

[a] State Key Laboratory of Robotics and System, Harbin Institute of Technology, Harbin, 150001, China
[b] School of Water Conservancy and Civil Engineering, Northeast Agricultural University, Harbin, 150030, China
[c] Center for Lunar and Planetary Sciences, Institute of Geochemistry, Chinese Academy of Sciences, Guiyang, 550081, China
[d] Light Industry College, Harbin University of Commerce, Harbin, 150001, China
[e] Beijing Institute of Spacecraft System Engineering, Beijing, 100094, China

ARTICLE INFO

Keywords:
Icy lunar regolith
Sample preparation
Nuclear magnetic resonance
Unfrozen water
Soil freezing characteristic curve

ABSTRACT

Water distribution uniformity is an important control criterion for icy lunar regolith samples during ground simulations and is easily influenced by the sample freezing process. However, the freezing process and characteristics of icy lunar regolith are rarely studied. Therefore, to address this issue, simulated samples of icy lunar regolith with two raw material ratios, various water contents and dry densities were prepared in this study, and the unfrozen water contents of samples at different freezing temperatures were tested by nuclear magnetic resonance instrument. The freezing process of icy lunar regolith from 20 °C to −192.8 °C was analyzed based on the variation of the T_2 spectrum, and the influence of initial water content and dry density of the samples on the variation rules of unfrozen water content with temperature was discussed. The results show that the freezing process includes the subcooling stage, the fast freezing stage, the slow freezing stage and the stable freezing stage. Below −80 °C, the unfrozen water content in both unsaturated and saturated samples reaches a very small order of magnitude. However, at −190 °C, unfrozen water is still present in the pores (<1 nm) of the samples. Unfrozen water can be divided into bound water, capillary water and gravity water. Unfrozen water in samples with the water content of 5 wt% and 10 wt% is mainly bound water, and water migration occurs during freezing. The solid ice formed during the freezing process of saturated samples has similar adsorption or capillary effect on unfrozen water to rock particles. A lower dry density of the sample means a higher initial freezing temperature and can more significantly promote the formation of capillary and gravity water. Finally, a new freezing characteristic model was constructed based on the linear relationship between particle and pore radii. The model well predicts the four variation stages of unfrozen water content with temperature from room temperature (20 °C) to extreme low temperature (−190 °C). And the applicability of the model was verified by quantifying the available surface permafrost data.

1. Introduction

Ground simulants are necessary for the physical analysis of icy lunar regolith (ILR) and the ground test validation on the payload of lunar landing and exploration [1–12]. The ground-based preparation of ILR samples has been conducted by many researchers [6,13–16]. Most of these researchers recognized the importance of water homogeneity to sample preparation and therefore adopted mechanical agitation [6, 13–15] or prolonged the sealing time [6,16] to ensure uniform distribution of water before sample freezing. Subsequently, the samples were frozen to the target temperature using liquid nitrogen or ultra-low temperature refrigerators. However, the impact of the sample freezing process on water homogeneity and evolution is neglected in these studies. According to the theory of permafrost physics, freezing of water-bearing soils is a typical multi-physical field coupling process [17], accompanied by phase change, migration and freezing expansion of water, which significantly influence the homogeneity of both sample structure and water distribution.

The soil freezing characteristic curve (SFCC, also known as the soil freezing characteristic model) is critical to analyzing the multi-field coupling effect of the freezing process and to further studying the

* Corresponding author.
E-mail address: jiangshy@hit.edu.cn (S. Jiang).

https://doi.org/10.1016/j.actaastro.2022.11.004
Received 10 June 2022; Received in revised form 26 October 2022; Accepted 3 November 2022
Available online 5 November 2022

Abbreviations

ILR	icy lunar regolith
SFCC	soil freezing characteristic curve
NMR	nuclear magnetic resonance
SWCC	soil-water characteristic curves
BCC	bundle of cylindrical capillary
CPMG	Carr–Purcell–Meiboom–Gill

water homogeneity of samples [17,18]. The SFCC indicates the relationship between unfrozen water content and temperature during sample freezing and can be obtained by various technical means, such as differential scanning calorimetry [19,20], time-domain reflectometry [21,22] and nuclear magnetic resonance (NMR) methods [23–26], etc. Among them, the NMR method has become more popular with its fast response, accurate signals and nondestructive measurement [27–32]. However, according to our knowledge, this technique has not been applied in the ILR simulant research. In terrestrial permafrost, theoretical prediction models have been successively proposed by domestic and foreign scholars, which can be roughly divided into three categories. The first category, empirical formulas summarized based on experimental data, is represented by the power function model proposed by Anderson and Tice [33]. In addition, some researchers modified the power function formulas or proposed new exponential function formulas and segmented function formulas [34–37]. These formulas are simple in form and widely applied. However, the fitted parameters of these models often lack practical physical significance. In the second category, the idea of analogy is utilized to approximate the equivalent SFCC using soil-water characteristic curves (SWCC) [38–43]. This is because, for water-bearing soils, freezing and drying are similar physical processes, both of which can be viewed as replacing liquid water with another phase [44]. However, Ma et al. measured SWCC and SFCC of silt and clay and found no similarity [45]. Azmatch et al. found significant differences between SWCC and SFCC of the specimen with salinity [46]. In addition, Ren and Vanapalli suggested that the drying and freezing processes may be fundamentally different [44]. For example, the way ice replaces water may be different from the way air replaces water in soil [47]. In the third category, the bundle of cylindrical capillary (BCC) model is used to simplify porous media. The Gibbs-Thomson equation is adopted to analyze the relationship between the capillary pore size and the decreased value of melting point temperature of the pore fluid. Subsequently, the pore characteristics of porous media were determined. For example, when studying the unfrozen water behavior during the freeze-thaw of pulverized clay, medium sand, and fine sand with different initial water contents and dry densities, Li et al. directly chose a probability density distribution function of pore radius without giving specific reason [17]. In a freezing characteristic model study of Tibetan powdered clay and bentonite mixtures with different specific surface areas, Liang referred to the research results of Wang et al. and chose the Weibull function as the probability distribution model of pore radius, without clarifying the reason of the choice based on the physical nature [48,49]. The freezing characteristic models obtained by the above three methods are for clay, sand or other categories of ground permafrost, which are fundamentally different from ILR in terms of mineral composition, particle morphology and particle size distribution. In addition, the temperatures of interest for ground permafrost is often around −30 °C, and the lowest is around −80 °C. This is much higher than the stable existence temperature of ILR (about −160 °C). That is, there is a lack of experimental and theoretical validation on the direct application of freezing characteristic model associated with surface permafrost to the ILR simulation samples.

In summary, the freezing pattern of liquid water and its effect on the samples in the field of ILR simulant preparation are neglected, and there is a lack of special objects with extreme low temperatures similar to ILR in the field of terrestrial permafrost for reference. Therefore, to prepare the ILR simulated samples with higher homogeneity, we first prepared simulated samples of ILR with different water content and dry densities and conducted NMR tests on these samples under different temperature conditions to analyze their freezing pattern based on the changes in T_2 spectrum. The effects of water content and dry densities on the freezing characteristics of the samples were analyzed based on the SFCC obtained from the experiments. Subsequently, the ILR simulation samples were simplified using the BCC model. The cumulative distribution function describing the pore radius of the sample was given according to the relationship between the particle size distribution and the pore radius distribution of the sample. The relationship between freezing temperature and pore radius was established based on the Gibbs-Thomson equation to construct a model of extreme low-temperature freezing characteristics applicable to ILR. Finally, the applicability of the model was verified using the data from this study and the existing permafrost data.

2. Materials and methods

2.1. Sample preparation and nuclear magnetic resonance test method

Basalt simulated lunar soil and anorthosite simulated lunar soil were selected as two basic raw materials, the former being the simulated lunar soil for Chang'e 5 ground drilling and sampling and the latter being the lunar highland simulant for Chang'e 7 ground testing. The ratio of the mass of basalt simulated lunar soil to the total sample mass is called the feedstock ratio C. The particle size distribution curves of the two feedstocks with different ratio factors are shown in Fig. 1.

The samples with different water contents and dry densities were prepared using the preparation method of indoor remodeled soils. Firstly, the raw materials were dried at 105–110 °C for 8 h to remove the initial water. Secondly, the determined mass of industrial distilled water was mixed with the dried simulated lunar soil according to the target water content. During the mixing process, the water was spread evenly in layers on the simulated lunar soil using a water spray bottle and stirred evenly using a stirrer. The mixed samples were sealed in bags for 24 h to ensure water homogeneity. Then, they were compacted in Teflon specimen tubes and wrapped with polyethylene film for sealing. Finally, the compacted samples were frozen or put directly into the NMR machine for test.

The T_2 curve obtained from the NMR test contains most of the physical information of the porous media, so it is the main target of the test. For porous media such as rocks and soils, there are mainly three

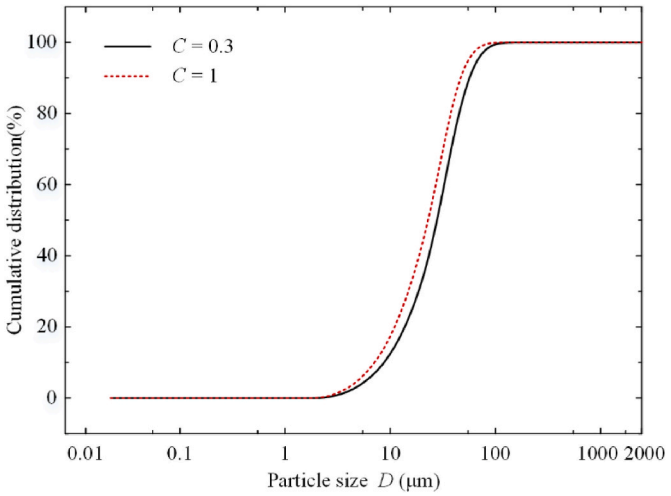

Fig. 1. Particle size distribution curves.

different relaxation mechanisms for fluids in their pores, and they exist simultaneously, which can be expressed as:

$$\frac{1}{T_2}=\frac{1}{T_{2f}}+\frac{1}{T_{2s}}+\frac{1}{T_{2d}}\approx\frac{1}{T_{2s}}=\rho_2\left(\frac{S}{V}\right)_{pore}=\rho_2\frac{F_s}{r} \quad (1)$$

where T_2 is the transverse magnetization vector decay time in s. T_{2f}, T_{2d} and T_{2s} represent free relaxation, diffusive relaxation and surface relaxation, respectively, in s. The first two are much smaller relative to the latter and are often neglected [50–52]; ρ_2 is the surface relaxation rate corresponding to T_2 in μm/s; S/V denotes the ratio of pore specific surface area to pore volume in μm^{-1}; F_s is the pore shape factor, and the values corresponding to spherical, cylindrical and planar pores are 3, 2 and 1, respectively; r is the pore radius in μm. From Equation (1), it is known that T_2 is inversely proportional to the specific surface area and directly proportional to the pore radius. When the sample is saturated, the pores are filled with liquid water, and the distribution of T_2 responds to that of liquid water in the pores of porous media.

Fig. 2 shows the Niumag MesoMR12-060H–I, the medium-size MRI analyzer used in this study, mainly consisting of a vacuum pressurized saturation unit, an industrial control computer, a magnet cabinet, a low-temperature heat exchange circulation system and a refrigeration heating circulation unit. The instrument can realize online regulation and control of sample temperature, and the temperature control range is −50 to 45 °C with an accuracy of ±0.1 °C. The frequency of the magnet was set at 12 MHz during the test, and the temperature was kept at 32 ± 0.01 °C to ensure the uniformity and stability of the magnetic field. The frequency control accuracy of the instrument is 0.1 Hz, and the pulse accuracy is 100 ns. The ambient temperature is 25 ± 3 °C during the test to reduce the environment influence on the test accuracy. The T_2 spectra of the samples at different temperatures were obtained in Carr–Purcell–Meiboom–Gill (CPMG) sequence tests.

The 12 samples used in the NMR experiments of this study are shown in Table 1 and are divided into three groups. The first group of samples S_1 and S_2 were unsaturated sample, and the temperature control unit of the NMR instrument was used to cool down the samples online. After the sample temperature was stabilized at the set value, the loading test could be performed, and the T_2 relaxation curves of the samples at this temperature condition could be obtained. The second group of samples S_2–S_8 were also unsaturated samples. Since the temperature control unit that comes with the NMR instrument cannot reach −196 °C, a step-by-step gradient cooling was used for these samples. First, the temperatures of samples were lowered from room temperature to −80 °C using an ultra-low temperature refrigerator, and then from −80 °C to −196 °C using liquid nitrogen. Since the sample temperature was far lower than the temperature control range of the instrument itself, constant control of the sample temperature was impossible. To ensure the test accuracy as much as possible, a sample (calibration sample) with a temperature sensor was prepared before the test, with its size, raw material ratio, water content and dry density the same as the sample under test. In addition, it was always kept at the same temperature conditions. When the NMR test was performed on the sample, the temperature of the companion on the sensor was read and used as the actual test temperature of the sample under test. The accuracy of the PT100 temperature sensor is $\pm(0.15 + 0.002\,|T|)$°C, and T indicates the temperature in °C. Since a single test could be completed within 10 s, the sample temperature did not change much during the whole process, so it is feasible to monitor and record the sample temperature under test based on the companion. After S_2, S_6 and S_8 have been tested at all temperature points and warmed up naturally to room temperature, the three samples were then placed in the vacuum pressurized saturation device in Fig. 3 for 24 h. The water-saturated samples were recorded as $S_{2\text{-}1}$, $S_{6\text{-}1}$ and $S_{8\text{-}1}$, respectively, as the third group of samples. In this way, the three samples with S_2, S_6 and S_8 have corresponding dry densities. When the effect of one freeze-thaw cycle on the internal pore structure of the samples was ignored, S_2 and $S_{2\text{-}1}$, S_6 and $S_{6\text{-}1}$, and S_8 and $S_{8\text{-}1}$ could be regarded as having the same pore morphology, size and

Table 1
Sample parameters.

Number	Raw material proportioning C	Water content (wt %)	Dry density (g/cm^3)	Temperature range
S_1	0.3	10	1.39	room temperature
S_2	0.3	10	1.29	to −30 °C
S_3	0.3	5	1.37	room temperature
S_4	0.3	5	1.43	to −196 °C
S_5	0.3	5	1.55	
S_6	0.3	5	1.71	
S_7	1	5	1.53	
S_8	1	10	1.60	
S_9	1	10	1.50	
$S_{3\text{-}1}$	0.3	29.9	1.37	room temperature
$S_{7\text{-}1}$	1	24.4	1.53	to −80 °C
$S_{9\text{-}1}$	1	23.5	1.50	

Fig. 2. MesoMR12-060H–I medium-size MRI analyzer (1) vacuum pressurized saturation unit; (2) industrial control machine; (3) magnet cabinet; (4) low-temperature heat exchange circulation system; (5) refrigeration heating circulation unit; (6) samples used in the test.

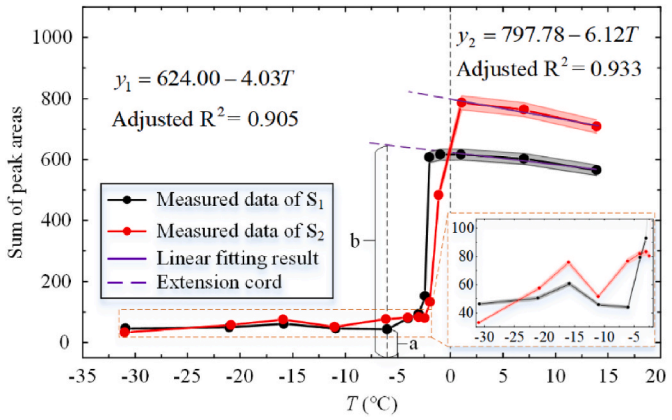

Fig. 3. Unfrozen water content calculation correction.

spatial distribution, while only the initial water content was different.

2.2. Calibration of unfrozen water content

In this study, the T_2 spectral peak area was used to quantify the unfrozen water content in the pores. Meanwhile, the effect of temperature on the NMR signal intensity was considered. Curie's law was chosen to correct for the temperature, and the measured peak area in the positive temperature interval was fitted using a linear function and extended to the negative temperature interval to obtain a paramagnetic linear regression line. The fitting equation is

$$y = \alpha + \beta T \tag{2}$$

where y denotes the sum of the peak areas and is a dimensionless value. T denotes the temperature of the sample in °C. α is the intercept at 0 °C and is a dimensionless value. β is the slope of the line in $°C^{-1}$ [25].

Fig. 3 shows the relationship between the sum of peak areas and temperature. Among them, the total peak area is directly measured by the instrument, and the maximum relative standard deviation is 3%. In the positive temperature interval, the sum of peak areas increases with decreasing temperature. When the temperature is near 0 °C, it starts to decrease, indicating that the water in the sample starts to freeze into ice. In the negative temperature region, the unfrozen water content is solved using a proportional calculation [53]. That is, the ratio of the measured value of the peak area at a certain negative temperature (value a) to the fitted value on the paramagnetic linear regression line at that temperature (value b) is used as a coefficient and then multiplied by the initial water content, as shown in Equation (3).

$$\theta_u = \frac{a}{b}\theta_0 \tag{3}$$

where θ_u is the unfrozen water content in wt%. θ_0 is the initial water content in wt%. Further, the accuracy of the measurements and the possible deviation of the experimental points need to be assessed [54]. In indirect measurement, the function of the measurement result is generally a multivariate function, and the equation is

$$U = f(u_1, u_2, \cdots, u_n) \tag{4}$$

where $u_1, u_2, \cdots, u_n$ is the directly measured value of each variable, and U is the value obtained by indirect measurement.

The error transfer equation is [55].

$$\frac{\Delta U}{U} \approx \frac{\partial f}{\partial u_1}\frac{\Delta u_1}{U} + \frac{\partial f}{\partial u_2}\frac{\Delta u_2}{U} + \cdots + \frac{\partial f}{\partial u_n}\frac{\Delta u_n}{U} \tag{5}$$

Therefore, substituting Equation (3) into Equation (5), the total error of unfrozen water content can be obtained as

$$\frac{d\theta_u}{\theta_u} = \frac{da}{a} + \frac{d\theta_0}{\theta_0} - \frac{d\alpha}{\alpha+\beta T} - \frac{Td\beta}{\alpha+\beta T} - \frac{\beta dT}{\alpha+\beta T} \tag{6}$$

where the first term on the right side of Equation (6) is provided by the NMR measurement instrument. The numerator of the second term indicates the error introduced by the manual sample preparation with a maximum of 0.2 wt%. The third and fourth terms indicate the error introduced by the fitting parameters. The last term is the error introduced by the temperature sensor measurements.

3. Results and discussion

3.1. T_2 spectrum analysis

The T_2 relaxation times of the samples at different temperatures are the direct data obtained from the NMR tests. When the pores of the porous medium are assumed to be cylindrical, the pore value can be obtained from Equation (1)

$$r = 2\rho_2 T_2 \tag{7}$$

In other words, T_2 is only related to the surface relaxation rate and the radius r of the capillary. When the surface relaxation rate is assumed to be constant, the T_2 distribution of the sample during the freezing process reflects liquid water variations in the sample pores at different scales with temperature. Therefore, to investigate how water freezes during the freezing process of the ILR simulation sample and the final freezing state, the effects of temperature, initial water content and density on the freezing process were analyzed qualitatively. This study draws on the results of Dunn et al. [56]: the surface relaxation rate of sand ranges from 0.3 to 46 μm/s, and that of the ILR simulation sample is assumed to be 50 μm/s. This assumption has been applied in the study of Kong et al. [34].

To investigate the effects of temperature, initial water content and dry density on the freezing process of the samples, typical samples S_3, $S_{3\text{-}1}$, S_7, $S_{7\text{-}1}$, S_8 and S_9 were selected for T_2 spectrum analysis as shown in Fig. 4. The T_2 cutoff values are widely used to distinguish bound fluids from free fluids in research fields such as petroleum reservoirs, coal reservoirs and NMR logging. According to Sondergeld et al. [57], the interval of T_2 greater than 33 ms corresponds to gravity water, the interval of T_2 less than 3 ms means bound water, and the interval between 3 ms and 33 ms indicates capillary water. The combination of these two cutoff values and Equation (7) showed that most liquid water in the unsaturated samples (S_3, S_7, S_8, and S_9) is bound water in pores smaller than ~0.3 μm, and the remaining small amount of water is capillary water and gravity water. The percentage of capillary and gravity water in sample S_3 is significantly higher than that of the remaining three unsaturated samples, which can be attributed to the smaller dry density of S_3. Thus, the porosity and pore size of S_3 is relatively larger, and the generation of capillary and gravity water is promoted. This phenomenon is more evident in the comparison of saturated samples $S_{3\text{-}1}$ and $S_{7\text{-}1}$.

From the overall view of Fig. 4(a)–(f), the NMR signal intensity gradually decreases with the decrease of temperature in the negative temperature interval, reflecting the gradual freezing of water in the pores. In addition, it can be seen from Fig. 4(b) that the content of bound water, capillary water and gravity water all decreased during the cooling process, and did not show the characteristic of freezing in the order of gravity water, capillary water and bound water. Equation (8) is the Gibbs-Thomson equation, which describes the relationship between pore radius and pore water freezing temperature and can be used to explain the above phenomenon [17,58].

$$T = T_0\left(1 - \frac{\gamma}{\rho_i L_a r}\right) \tag{8}$$

where T_0 is the melting point of water, 273.15 K, γ is the free energy at the solid ice-liquid water interface, 0.0818 J/m^2, L_a is the latent heat of

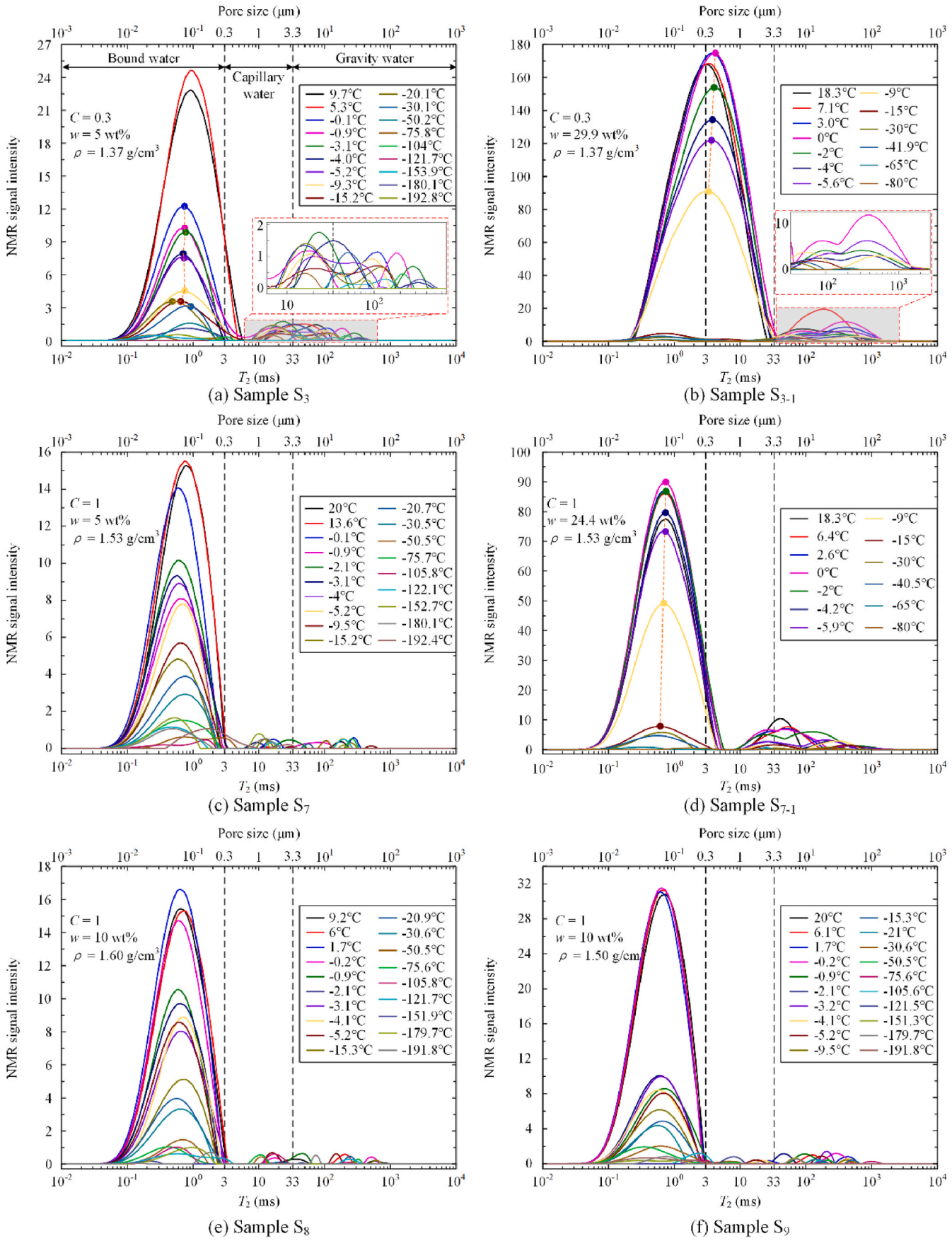

Fig. 4. Variations of T_2 distribution curves with temperature for different samples.

the solid per unit mass, 334.56 kJ/kg, ρ_i is the density of ice, 917 kg/m^3, r is the pore radius and T is the freezing temperature of water in a pore of radius r in K.

Fig. 5 shows the freezing temperature variation with pore radius, which is plotted according to the Gibbs-Thomson equation. It can be seen that when the pore radius $r \geq 3.3\mu$m, the freezing temperature of gravity water in the pore is basically unaffected by the pore; when the pore radius $0.3 < r < 3.3\mu$m, the freezing temperature of capillary water in the pore is less affected by the pore radius, and the temperature value reduction is within 0.5 °C. For bound water ($r < 0.3\mu$m), the freezing temperature reduction effect of nanoscale pores is strong, but that of 0.1–0.3 μm scale pores is insignificant (<1 °C). That is when the sample temperature decreases to −1 °C, the bound, capillary, and gravity water in pores larger than 0.1 μm all freeze, which explains the non-sequential freezing of the three kinds of unfrozen water in Fig. 4(b). If sequential freezing is desired, the smaller temperature control gradients should be adopted, which is often difficult in practice applications. It can be seen from Fig. 4(b) and (d) that when the temperature is reduced to −15 °C, the water in the sample is basically unfrozen bound water. At this time, the first peak of the T_2 spectrum is located exactly on the left side of T_2 = 3ms, which also indicates that the choice of 3 ms as the cut-off value to distinguish bound water from capillary water is reasonable.

By comparison, only the initial water content of the two samples in Fig. 4(a) and (b) is different, and their dry density is 1.37 g/cm^3, which is smaller than that of other samples. The water saturation behavior not only significantly increased the amplitude of the NMR signal intensity, but also increased the proportion and content of capillary and gravimetric water in the samples. During the freezing process, the characteristics of the two samples are significantly different: first, on the whole, the peaks of the T_2 curves of both saturated sample $S_{3\text{-}1}$ and unsaturated sample S_3 gradually decrease as the temperature decreases (negative temperature interval). The first peak of the T_2 spectral curve of the saturated sample $S_{3\text{-}1}$ shifts to the left, while that of unsaturated sample S_3 shows a left-right oscillation. This feature is also evident in the rest of the samples. In this study, the reason is that the water in the unsaturated sample may not have wetted each rock particle sufficiently and local water migration occurred during the freezing process. The T_2 distribution curve of saturated sample $S_{3\text{-}1}$ in the positive temperature interval should reflect all the pore distribution characteristics of these two samples when the effect of one freeze-thaw cycle on the pore state of the samples is ignored. According to the T_2 distribution curve of $S_{3\text{-}1}$, the pores in the S_3 sample were not completely filled, but capillary water and gravity water existed in the large local pores of S_3, which indicated that the water did not make all particles in the sample uniformly and completely wetted. According to the theory of thin-film water migration, unfrozen water in the sample pores will migrate toward the cold front during the freezing process, and this dynamic feature will also lead to a non-directional transverse shift of the first peak of the T_2 spectral curve. Second, the local zoomed-in plots in Fig. 4(a) and (b) contain only the T_2 distributions in the negative temperature interval. The comparative analysis shows that the T_2 distribution of saturated sample $S_{3\text{-}1}$ variates regularly, while that of the unsaturated sample S_3 showed irregular changes, which is possibly caused by water migration. However, because of the low NMR signal intensity of free water (capillary and gravity water) in the local amplification region, the humidity of the test environment may possibly play a role. To determine the real reason of this phenomena, a Teflon specimen tube (without sample) was wrapped with the same polyethylene film and placed in liquid nitrogen for frozenness. The test tube was tested after the temperature of the specimen tube was lowered to −190 °C. The entire test process and test parameters were kept consistent with those of the sample, and the test results are shown in Fig. 6. According to this figure, the effect of ambient humidity on the test is small and mainly occurs in the interval of $T_2 < 3$ ms, corresponding to the T_2 interval of capillary water and gravity water basically does not affect this phenomenon. Therefore, this study attributes this difference to the localized water migration that occurred in the unsaturated samples.

The two samples in Fig. 4(c) and (d) have the same raw material ratio and dry density but different initial water content. On the whole, the same differential characteristics as the two samples S_3 and $S_{3\text{-}1}$ are exhibited. However, $S_{7\text{-}1}$ has a lower capillary to gravimetric water ratio than $S_{3\text{-}1}$ because of the greater dry density of sample $S_{7\text{-}1}$, which also results in the smaller pore size of sample $S_{7\text{-}1}$. The comparison of samples S_8 and S_9 shows that they have the same raw material ratio and water content and different dry densities. Their NMR signal intensity is significantly reduced at −0.9 °C, but the decreasing effect of S_9 is more pronounced because of its smaller density and larger pore scale. According to the Gibbs-Thomson equation, a larger pore size corresponds to a higher freezing temperature. Therefore, the S_9 sample would also have a more pronounced NMR signal intensity decrease at −0.9 °C.

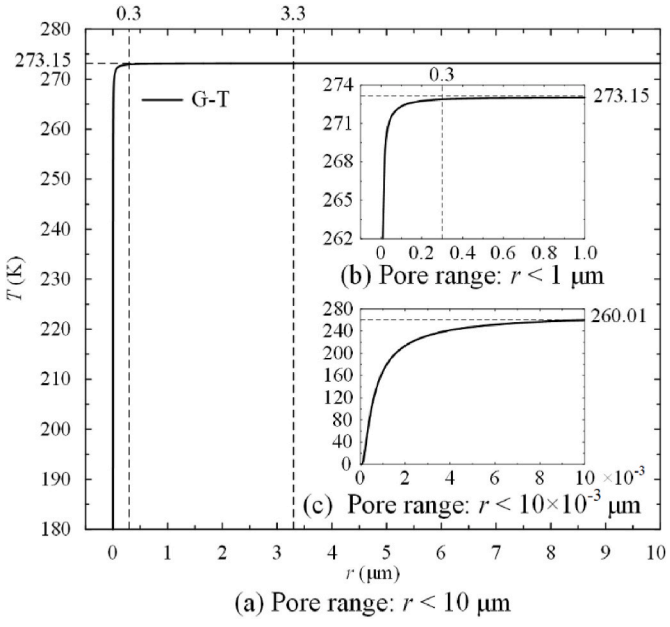

Fig. 5. Correspondence between pore water freezing temperature and pore radius.

3.2. Variation of total unfrozen water content with temperature

According to Equation (3) and Equation (6), some typical samples were selected to plot Fig. 7 to analyze the variation pattern of unfrozen water content with temperature, and factors such as dry density and initial water content were introduced for consideration. Fig. 7(a) shows

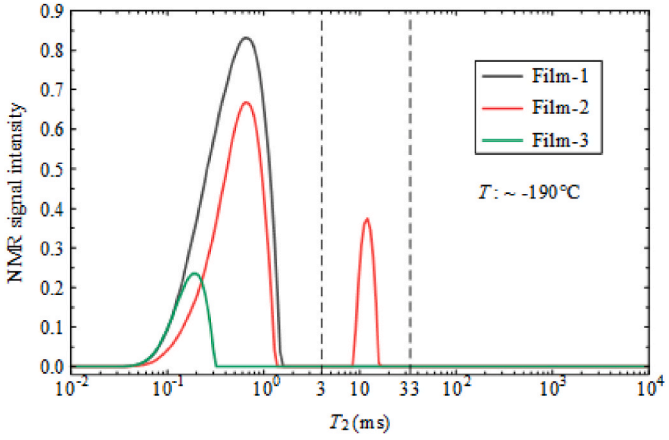

Fig. 6. Analysis of the effect of humidity on the test environment.

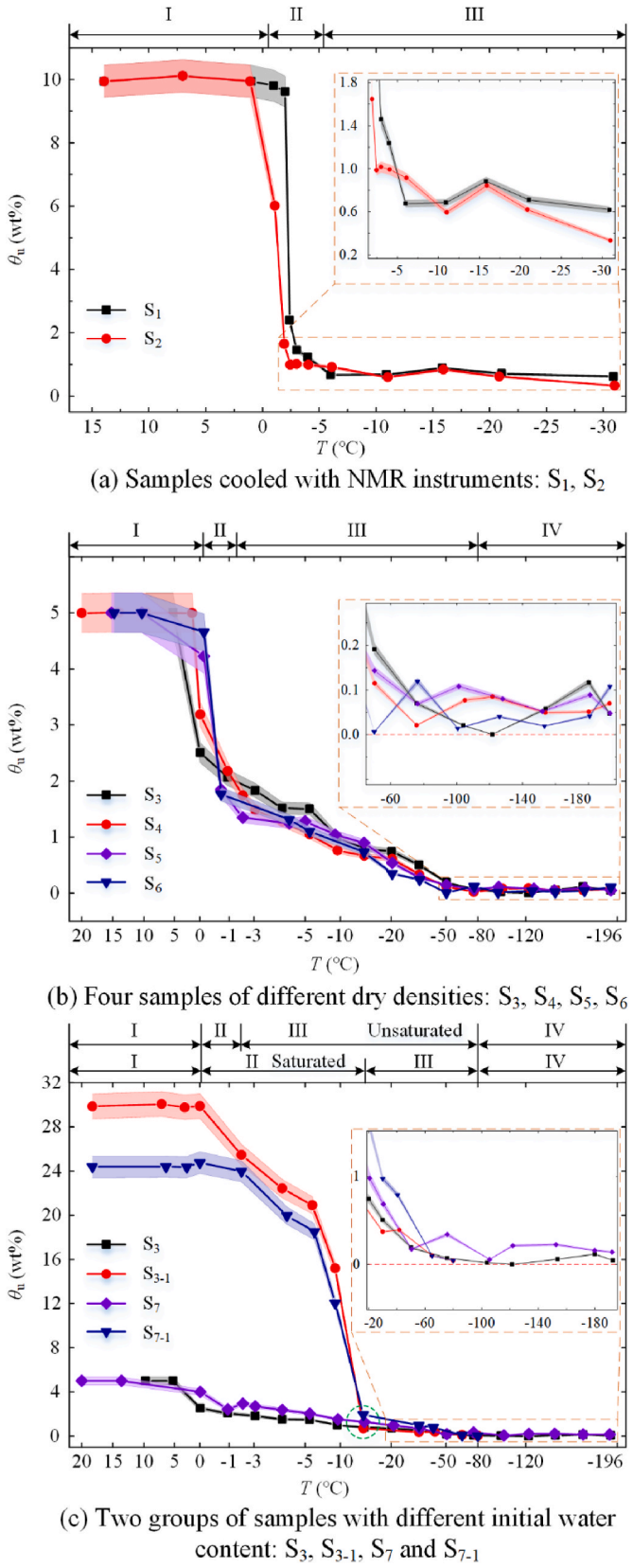

(a) Samples cooled with NMR instruments: S_1, S_2

(b) Four samples of different dry densities: S_3, S_4, S_5, S_6

(c) Two groups of samples with different initial water content: S_3, S_{3-1}, S_7 and S_{7-1}

Fig. 7. Variation of total unfrozen water content with temperature.

two samples under continuous cooling using the temperature control unit of the NMR instrument. Fig. 7(b) shows four unsaturated samples that are only different in dry densities. Fig. 7(c) exhibited the comparison of the effect of different initial water contents on the variation of unfrozen water content with temperature.

According to Fig. 7(a), the samples underwent three stages during the freezing process: I. Subcooling stage; II. Rapid freezing stage; III. Stable freezing stage, which is generally consented by the scholars in the field of permafrost. In stage II (this stage starts at the sample's starting freezing temperature T_f, which is equal to or slightly lower than the freezing temperature of pure water), the unfrozen water content of sample S_1 is overall higher than that of sample S_2, and the temperature where the unfrozen water content of S_1 is suddenly dropped is significantly lower than that of S_2. This is because sample S_1 has a larger dry density. This means that the smaller the size of the pores, the lower the freezing temperature required. In Stage III, the unfrozen water content of samples S_1 and S_2 were essentially comparable and did not change significantly as the temperature decreased. However, during the freezing of the ILR simulated samples to −196 °C by liquid nitrogen in this study, it was found that the samples underwent four stages: I. Subcooling section; II. Fast freezing section; III. Slow freezing section; IV. Stable freezing section (or non-freezable section), which is shown in Fig. 7(b) and (c).

The four samples in Fig. 7(b) have the same water content and raw material ratio and different dry densities. On the whole, the trend of unfrozen water content with temperature is the same for these four samples. However, as the dry density increased, the starting freezing temperatures of the four samples S_3, S_4, S_5, and S_6, decreased sequentially. In addition, another remarkable feature is that the unfrozen water content of these four samples is all slightly greater than 0 below −80 °C, which is possibly because of two reasons: first, it can be seen from Fig. 5 that pores <1 nm at −190 °C can still provide for the presence of liquid water, even though the content of pore water may be very low; second, it can be seen from Fig. 6 that water vapor in the surrounding environment influences the total unfrozen water content of the test.

From Fig. 7(c), it can be seen that the freezing processes of saturated and unsaturated samples are also characterized by four stages, but they are significantly different, mainly in that the end temperature of the fast-declining section II of the former is much lower than that of the latter. In addition, the total unfrozen water content of the two types of samples at −15 °C was not significantly different. Moreover, the SFCC of the two samples is more convergent as the temperature decreases. This is because the capillary and gravimetric water in the saturated samples at −15 °C can be considered as completely frozen, and the remaining amount of unfrozen bound water is comparable to that of the unsaturated samples. In other words, regardless of the initial water content, their SFCC will not be affected by the initial water content when the sample temperature is reduced to a certain negative value.

3.3. Content variation of each type of unfrozen water with temperature

The unfrozen water in the samples can be classified into bound water, capillary water and gravity water using the T_2 cutoff value, and the freezing patterns of these unfrozen water within the samples can be obtained based on the T_2 distribution curves during freezing, as shown in Fig. 8. As a whole: first, the unfrozen water in the unsaturated samples S_3 and S_9 is essentially in the form of bound water, with a little capillary and gravity water; second, although bound water still occupies a significant proportion in the saturated samples S_{3-1} and S_{9-1}, the increase in capillary water content in S_{3-1} is particularly pronounced, and the gravity water content in S_{3-1} and capillary water content in S_{9-1} also are also increased. In addition, there is more capillary and gravimetric water in sample S_{3-1} than in sample S_{9-1}, and even the capillary and bound water contents in S_{3-1} were comparable. This phenomenon can be attributed to the fact that samples with a smaller dry density will have a larger pore structure, promoting the formation of capillary and gravity

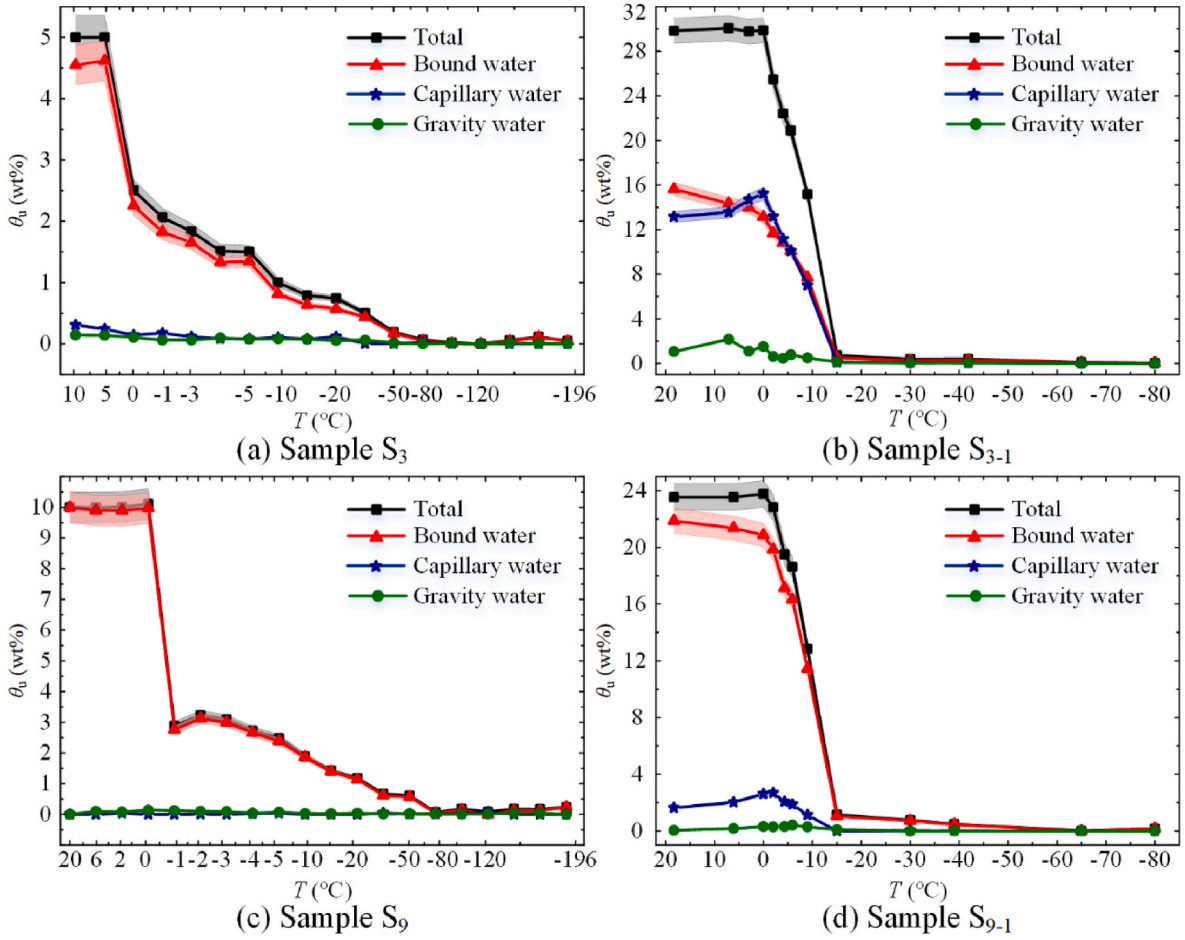

Fig. 8. Variation of various types of unfrozen water with temperature.

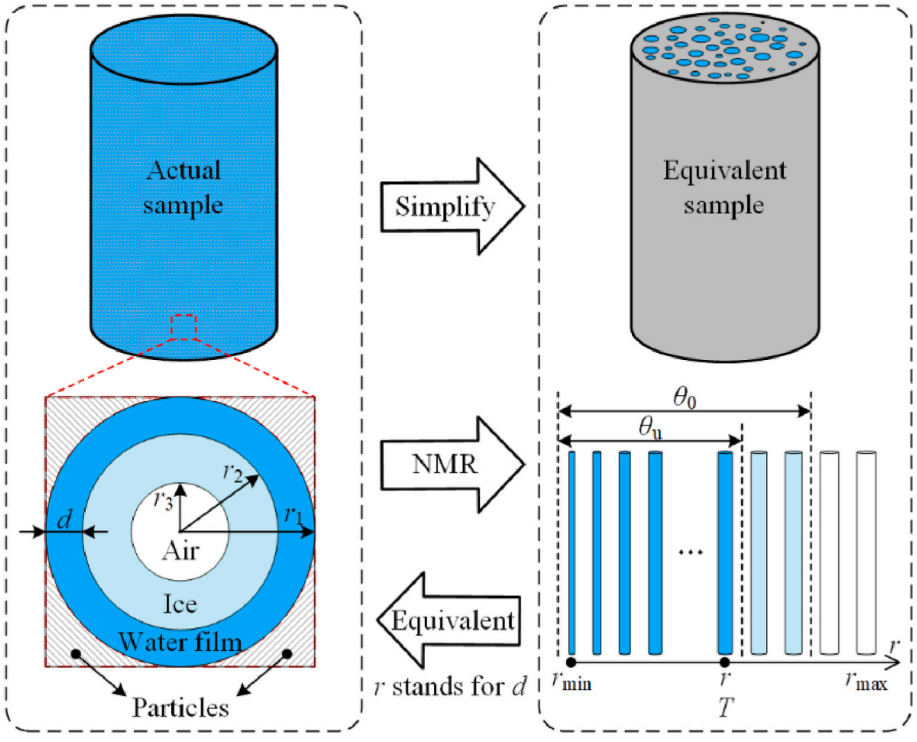

Fig. 9. Simplification of the icy lunar regolith simulation samples using the columnar capillary bundle model.

water; third, the freezing of the three kinds of unfrozen water occurred almost simultaneously, without sequential freezing. This can be explained by the relationship between freezing temperature and pore-scale in Fig. 5: when the temperature decreases to −1 °C, the temperature of bound water, capillary water and gravity water in the pore with a radius $r > 73$ nm all reach the freezing value. Therefore, the conclusion that the pore water freezes sequentially should be correct, except that the sample temperatures are set over too large a span to show this feature.

The pores of saturated samples $S_{3\text{-}1}$ and $S_{9\text{-}1}$ are filled with bound water, capillary water and gravity water. During the rapid freezing stage, the gravity water in the saturated samples was almost completely frozen, while the capillary water content started to decrease only after a slight increase. In this study, it is believed that the frozen solid ice changed the original pore structure, causing the original unfrozen water to change its category and properties, such as unfrozen gravity water to capillary water. In other words, the frozen formed ice has a similar adsorption and capillary effect on unfrozen water as rock particles. This leads to the increase of capillary water content in saturated samples during the rapid freezing phase.

4. Freezing characteristics model construction and verification

4.1. Model construction

The BCC model is chosen to simplify the simulated sample of ILR with porous media characteristics, as shown in Fig. 9, which have size and distribution characteristics. The sample shown in Fig. 9 is an unsaturated sample, and the radius of the pore surrounded by several particle walls in the actual sample is noted as r_1, and the pore is partially filled by water and air. During the freezing process, the liquid water freezes from the pore center towards the pore wall surface. At a certain freezing temperature T, the distance between the front surface of the frozen ice and the center of the pore is r_2, and the radius of the pore occupied by air is r_3. When $r_3 = 0$ μm, Fig. 9 can be used to represent saturated samples. At this time, the thickness of the unfrozen water film is d.

$$d = r_1 - r_2 \tag{9}$$

At the freezing temperature T, the samples were tested by NMR, and the pore size occupied by unfrozen liquid water can be obtained according to Equation (1) using T_2, which means that the water film thickness d is replaced by r equivalently. According to the Gibbs-Thomson equation, the freezing temperature and the pore radius have a one-to-one correspondence. Moreover, as the pore size decreases, the freezing temperature of pore water in porous media also decreases.

When $T \geq T_f$, the

$$\theta_u = \theta_0 \tag{10}$$

where T_f is the starting freezing temperature of the sample in K. θ_0 is the initial water content of the sample in wt%.

When $T < T_f$, only the water in the pores from r_{min} to r does not freeze, and the content of unfrozen water θ_u can be expressed as

$$\theta_u(r) = \theta_0 \int_{r_{min}}^{r} g(r)\,\mathrm{d}r = \theta_0[G(r) - G(r_{min})] \tag{11}$$

where $g(r)$ is the probability density function of pore radius and $G(r)$ denotes the cumulative distribution function of pore radius. Numerous researchers have demonstrated [18,59,60] that there is a linear proportional relationship between the pore radius of permafrost-like porous media and the radius of rock particles, as shown in Equation (12).

$$r_i = 0.3R_i \tag{12}$$

Where R_i is the average particle radius of the i-th fraction, and r_i is the corresponding equivalent pore radius. Therefore, the two-parameter Rosin-Rammler function describing the particle size distribution can be used in this study to represent the cumulative distribution of the sample pore radii, as shown in Equation (13).

$$G(r) = 1 - \exp\left[-\left(\frac{r}{r_e}\right)^m\right] \tag{13}$$

Where $G(r)$ denotes the negative mass accumulation rate, r_e represents the characteristic radius of the pores in μm, and its size is the radius of the pores at the time of $G(r) = 63.2\%$, and m is the distribution modulus. When r_{min} is equal to 0, the value of $G(r_{min})$ is equal to 0. Therefore, once m and r_e are determined, the distribution characteristics of the pore radius of the sample are ascertained. Combining Equations (8), (10), (11) and (13), the functional relationship between the unfrozen water content of the ILR simulation sample and temperature can be obtained as:

$$\theta_u(T) = \begin{cases} \theta_0 & T \geq T_f \\ \theta_0\left\{1 - \exp\left[-\left(\dfrac{T_0\gamma}{\rho_i L_a r_e (T_0 - T)}\right)^m\right]\right\} & T < T_f \end{cases} \tag{14}$$

where the unit of temperature T is K.

4.2. Model validation

The constructed freezing characteristic model, Equation (14), was used to validate the 12 samples of this study. The results are shown in Fig. 10 and Table 2. From Fig. 10, it is found that the calculated results are consistent with the experimental data. It can well show the freezing process characteristics of the samples at four stages and also reflect the differences caused by different densities.

To further verify the applicability of the model proposed in this study, the available experimental data were used for discussion and analysis. Table 3 shows the parameter information and fitting results for the six samples used. The first three samples had the same soil type and dry density ρ_d, and differed only in initial water content. Based on the fitted curves in Fig. 11(a) and the fitted results in Table 3, it can be seen that the proposed model has an ideal fit for loess with different initial water contents. Similarly, the proposed model has a good fit for the last three samples with different soil types and similar water contents. In summary, the model proposed in this study is applicable to both the analysis of freezing characteristics of ILR simulants and provides a new reference for the related research on Earth's permafrost.

5. Conclusion

In this paper, simulated icy lunar regolith samples with different ratios, dry densities and initial water contents were prepared using basalt simulated lunar soil and anorthosite simulated lunar soil. The freezing process of liquid water in the samples was investigated from room temperature to extreme low-temperature freezing using nuclear magnetic resonance technique. The effects of sample dry density and initial water content on the soil freezing characteristic curve of the icy lunar regolith simulated samples were compared and analyzed, and a new freezing characteristic model was proposed. This paper studies the effect of freezing during icy lunar regolith simulant preparation, which provides a theoretical basis for preparing samples with higher homogeneity. At the same time, the application of the freezing characteristics model is extended from terrestrial permafrost to lunar water detection, especially the temperature applicability range of the model. The following conclusions are drawn:

(1) The changes in unfrozen water content of the icy lunar regolith simulation samples from room temperature to extreme low-temperature freezing can be divided into the subcooling stage,

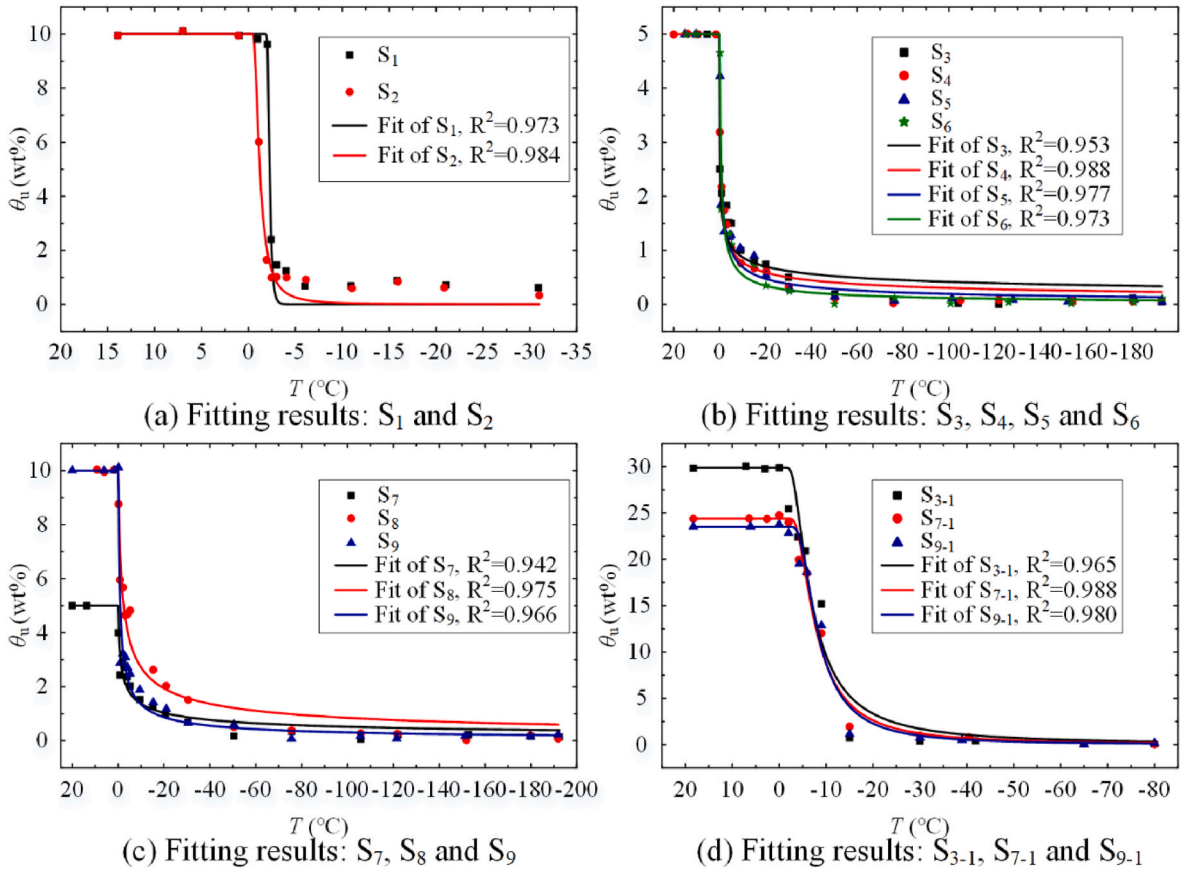

Fig. 10. Fitting results of the model proposed in this study.

Table 2
The fitted parameters and results of the model proposed in this study.

Number	r_e (μm)	m	Adjusted R^2
S_1	0.033	12.272	0.973
S_2	0.070	2.316	0.984
S_3	0.892	0.343	0.953
S_4	0.436	0.433	0.988
S_5	0.196	0.578	0.977
S_6	0.166	0.689	0.973
S_7	0.084	0.466	0.942
S_8	0.058	0.554	0.975
S_9	0.134	0.665	0.966
$S_{3\text{-}1}$	0.013	1.714	0.965
$S_{7\text{-}1}$	0.011	1.973	0.988
$S_{9\text{-}1}$	0.010	2.199	0.980

fast freezing stage, slow freezing stage, and stable freezing stage. In the fast freezing stage, the starting freezing temperature decreased as the dry density of the sample increased. Moreover, the end temperature of the fast-falling phase for saturated samples was much lower than that of unsaturated samples, but the soil freezing characteristic curve of both types of samples converged with the decrease in temperature. For the slow freezing stage, the unfrozen water content of both saturated and unsaturated samples reached the same small value below −80 °C. During the stable freezing stage, the unfrozen water content of the samples showed insignificant changes. Although the amount of unfrozen water in the sample is very small when the sample temperature is −190 °C, the <1 nm pores can still provide conditions for the presence of liquid water.

(2) Unfrozen water in the icy lunar regolith simulation samples include bound water, capillary water, and gravity water. In the simulated samples with the initial water content of 5 wt% and 10 wt%, the unfrozen water was mainly bound water, with a little capillary water and gravity water. Moreover, the smaller dry density of the samples with the same initial water content could better promote the formation of capillary and gravity water.

(3) The solid ice formed during freezing of saturated samples has an adsorption and capillary effect on liquid water, a property similar to the effect of rock particles on unfrozen water. This causes the

Table 3
Parameters and fitting results of the six samples used for model applicability assessment.

No.	Soil type	Soil parameters			Source	Fitting parameters and results		
		ρ_d (g/cm^3)	θ_0 (wt%)	T_f (°C)		r_e (μm)	m	Adjusted R^2
T-1	Loess	1.63	25.0	–	Tang et al. [61]	0.084	0.899	0.998
T-2			20.0	–		0.055	0.768	0.994
T-3			5.0	–		0.009	0.481	0.967
T-4	70% sand and 30% bentonite	1.7	19.0	−0.29	Kong et al. [34]	0.027	13.728	0.994
T-5	30% sand and 70%bentonite		21.0	−1.35		0.018	1.927	0.982
T-6	Pure bentonite		20.0	−1.86		0.011	1.389	0.992

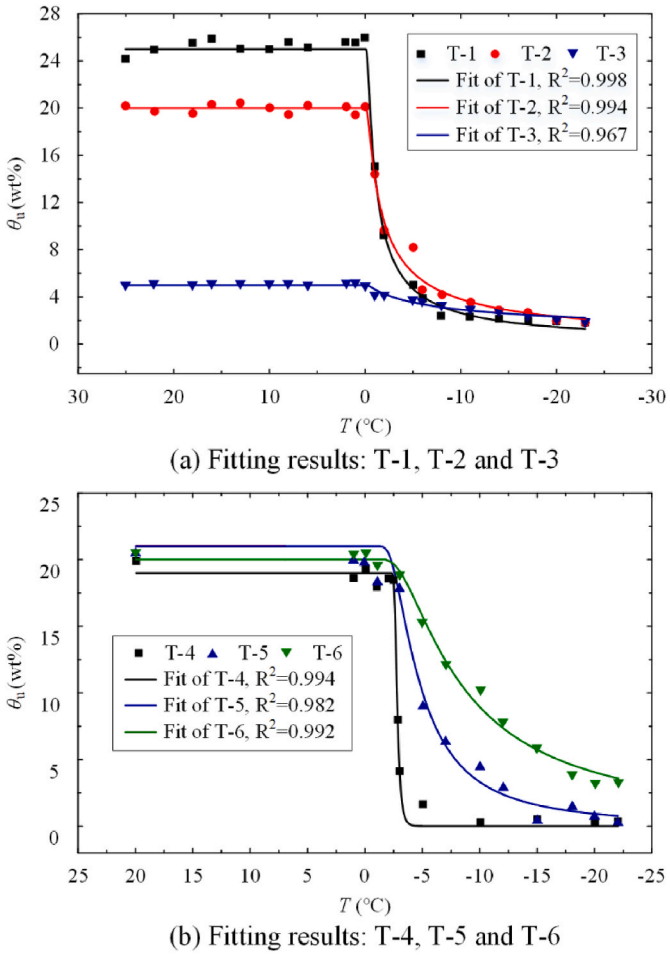

Fig. 11. Validation results of ground permafrost samples.

capillary water content in the saturated sample to show a slight increase during the rapid freezing stage. However, when the samples were frozen to a certain negative temperature, their soil freezing characteristic curve will be unaffected by the initial water content.

(4) The cumulative distribution function of the pore radius of the icy lunar regolith simulation sample was given based on the linear relationship between the particle radius and the pore radius, and then a new freezing characteristic model was constructed, which could fit all the measured data well. At the same time, it could show the freezing process characteristics of the samples at the four stages. Finally, the applicability of the model proposed in this study was verified using data from existing surface permafrost.

Declaration of competing interest

The authors declare that they have no known competing financial interests or personal relationships that could have appeared to influence the work reported in this paper.

Acknowledgments

This project is supported by the National Natural Science Foundation of China (Grant Nos. 52005136, U2013603).

References

[1] J. Biswas, S. Sheridan, C. Pitcher, L. Richter, M. Reganaz, S.J. Barber, P. Reiss, Searching for potential ice-rich mining sites on the moon with the lunar volatiles scout, Planet. Space Sci. 181 (2020), 104826, https://doi.org/10.1016/j.pss.2019.104826.

[2] L. He, C. Wang, G. Zhang, Y. Pang, W. Yao, A novel auger-based system for extraterrestrial in-situ water resource extraction, Icarus 367 (2021), 114552, https://doi.org/10.1016/j.icarus.2021.114552.

[3] K. Zacny, P. Chu, G. Paulsen, A. Avanesyan, J. Craft, L. Osborne, Mobile in-situ water extractor (MISWE) for Mars, Moon, and Asteroids in situ resource utilization, in: AIAA Sp. 2012 Conf. Expo, 2012, p. 5168.

[4] K. Zacny, D. Glaser, P. Bartlett, K. Davis, S. Gorevan, Drilling results in ice-bound simulated lunar regolith, in: AIP Conf. Proc, American Institute of Physics, 2007, pp. 838–845.

[5] D. Joshi, Real-Time Characterization of Water-Bearing Lunar Regolith while Drilling on the Moon, Colorado School of Mines, 2021. https://www.proquest.com/dissertations-theses/real-time-characterization-water-bearing-lunar/docview/2549678482/se-2?accountid=28855.

[6] D.R. Joshi, A.W. Eustes, J. Rostami, C. Dreyer, S. Nieczkoski, Material characterization while drilling on the moon: comparing the atmospheric and cryogenic drilling data, Accel. Sp. Commer. Explor. New Discov. Conf. ASCEND 2020 (2020) 1–10, https://doi.org/10.2514/6.2020-4147.

[7] D. Joshi, A. Eustes, J. Rostami, C. Gottschalk, C. Dreyer, W. Liu, Z. Zody, C. Bottini, How can drilling engineers help revolutionize space transport and colonize the solar system: focusing on lunar water-ice, Proc. - SPE Annu. Tech. Conf. Exhib. 2019-Septe (2019), https://doi.org/10.2118/195803-ms.

[8] J. Liu, W. Zhang, Y. Tian, L. Tao, P. Li, S. Jiang, Analysis and prediction of uniaxial compressive strength of icy lunar regolith under extreme temperature, Adv. Space Res. 69 (2022) 4391–4407, https://doi.org/10.1016/j.asr.2022.03.042.

[9] A. Ogishima, K. Saiki, Development of a micro-ice production apparatus and NIR spectral measurements of frosted minerals for future lunar ice exploration missions, Icarus 357 (2021), 114273, https://doi.org/10.1016/j.icarus.2020.114273.

[10] M. Piquette, M. Horányi, S.A. Stern, Laboratory experiments to investigate sublimation rates of water ice in nighttime lunar regolith, Icarus 293 (2017) 180–184, https://doi.org/10.1016/j.icarus.2017.04.017.

[11] T.L. Roush, A. Colaprete, A.M. Cook, R. Bielawski, E. Fritzler, J. Benton, B. White, J. Forgione, J. Kleinhenz, J. Smith, G. Paulsen, K. Zacny, R. McMurray, Volatile monitoring of soil cuttings during drilling in cryogenic, water-doped lunar simulant, Adv. Space Res. 62 (2018) 1025–1033, https://doi.org/10.1016/j.asr.2018.06.024.

[12] T.G. Wasilewski, T. Barciński, M. Marchewka, Experimental investigations of thermal properties of icy lunar regolith and their influence on phase change interface movement, Planet. Space Sci. 200 (2021), https://doi.org/10.1016/j.pss.2021.105197.

[13] R. Fisackerly, J. Carpenter, B. Houdou, G. Visentin, F. Rizzi, M. Savoia, P. Magnani, S. Barber, Accessing, drill and operating at the lunar south Pole: status of European plans and activities, in: 9th Symp. Sp. Resour. Util, American Institute of Aeronautics and Astronautics, 2016, https://doi.org/10.2514/6.2016-0224.

[14] J. Kleinhenz, D. Linne, Preparation of a frozen regolith simulant bed for ISRU component testing in a vacuum chamber, in: 51st AIAA Aerosp. Sci. Meet. Incl. New Horizons Forum Aerosp. Expo, 2013, p. 732.

[15] C. Pitcher, N. Kömle, O. Leibniz, O. Morales-Calderon, Y. Gao, L. Richter, Investigation of the properties of icy lunar polar regolith simulants, Adv. Space Res. 57 (2016) 1197–1208, https://doi.org/10.1016/j.asr.2015.12.030.

[16] J. Atkinson, M. Prasad, A. Abbud-Madrid, C.B. Dreyer, Penetration and relaxation behavior of JSC-1A lunar regolith simulant under cryogenic conditions, Icarus 346 (2020), 113812, https://doi.org/10.1016/j.icarus.2020.113812.

[17] Z. Li, J. Chen, M. Sugimoto, Pulsed NMR measurements of unfrozen water content in partially frozen soil, J. Cold Reg. Eng. 34 (2020), 4020013.

[18] C. Wang, S. Li, Y. Lai, Q. Chen, X. He, H. Zhang, X. Liu, Predicting the soil freezing characteristic from the particle size distribution based on micro-pore space geometry, Water Resour. Res. 58 (2022), e2021WR030782.

[19] T. Kozlowski, A comprehensive method of determining the soil unfrozen water curves: 1. Application of the term of convolution, Cold Reg. Sci. Technol. 36 (2003) 71–79, https://doi.org/10.1016/S0165-232X(03)00007-7.

[20] T. Kozlowski, A comprehensive method of determining the soil unfrozen water curves: 2. Stages of the phase change process in frozen soil-water system, Cold Reg. Sci. Technol. 36 (2003) 81–92, https://doi.org/10.1016/S0165-232X(03)00006-5.

[21] D.E. Patterson, M.W. Smith, The measurement of unfrozen water content by time domain reflectometry: results from laboratory tests, Can. Geotech. J. 18 (1981) 131–144, https://doi.org/10.1139/t81-012.

[22] M. Stähli, D. Stadler, Measurement of water and solute dynamics in freezing soil columns with time domain reflectometry, J. Hydrol. 195 (1997) 352–369, https://doi.org/10.1016/S0022-1694(96)03227-1.

[23] A.M. Kruse, M.M. Darrow, Adsorbed cation effects on unfrozen water in fine-grained frozen soil measured using pulsed nuclear magnetic resonance, Cold Reg. Sci. Technol. 142 (2017) 42–54, https://doi.org/10.1016/j.coldregions.2017.07.006.

[24] M. K A, M. D M, A. Satoshi, Improvements in measuring unfrozen water in frozen soils using the pulsed nuclear magnetic resonance method, J. Cold Reg. Eng. 32 (2018), 4017016, https://doi.org/10.1061/(ASCE)CR.1943-5495.0000141.

[25] A.R. Tice, D.M. Anderson, K.F. Sterrett, Unfrozen water contents of submarine permafrost determined by nuclear magnetic resonance, in: Dev. Geotech. Eng, Elsevier, 1982, pp. 135–146.

[26] K. Watanabe, T. Wake, Measurement of unfrozen water content and relative permittivity of frozen unsaturated soil using NMR and TDR, Cold Reg. Sci. Technol. 59 (2009) 34–41, https://doi.org/10.1016/j.coldregions.2009.05.011.
[27] B. Kong, S. He, T. Xia, Z. Ding, Research on microstructure of soft clay under various artificial ground freezing conditions based on nmr, Appl. Sci. 11 (2021) 1–19, https://doi.org/10.3390/app11041810.
[28] P. Lei, M.W. Young, J.D. Seymour, D.E. Stillman, K. Primm, H.G. Sizemore, A. W. Rempel, S.L. Codd, NMR Characterization of unfrozen brine vein distribution and structure in model packed beds, Cold Reg. Sci. Technol. 199 (2022), 103572, https://doi.org/10.1016/j.coldregions.2022.103572.
[29] J. Li, E. Ma, Characterization of water in wood by time-domain nuclear magnetic resonance spectroscopy (Td-nmr): a review, Forests 12 (2021), https://doi.org/10.3390/f12070886.
[30] Z. Su, X. Tan, W. Chen, H. Jia, F. Xu, A model of unfrozen water content in rock during freezing and thawing with experimental validation by nuclear magnetic resonance, J. Rock Mech. Geotech. Eng. (2022), https://doi.org/10.1016/j.jrmge.2021.10.009.
[31] T. Wang, Q. Sun, H. Jia, J. Ren, T. Luo, Linking the mechanical properties of frozen sandstone to phase composition of pore water measured by LF-NMR at subzero temperatures, Bull. Eng. Geol. Environ. 80 (2021) 4501–4513, https://doi.org/10.1007/s10064-021-02224-3.
[32] L. Weng, Z. Wu, Q. Liu, Z. Chu, S. Zhang, Evolutions of the unfrozen water content of saturated sandstones during freezing process and the freeze-induced damage characteristics, Int. J. Rock Mech. Min. Sci. 142 (2021), 104757, https://doi.org/10.1016/j.ijrmms.2021.104757.
[33] D.M. Anderson, A.R. Tice, Predicting unfrozen water contents in frozen soils from surface area measurements, Highw. Res. Rec. 393 (1972) 12–18.
[34] L. Kong, Y. Wang, W. Sun, J. Qi, Influence of plasticity on unfrozen water content of frozen soils as determined by nuclear magnetic resonance, Cold Reg. Sci. Technol. 172 (2020), 102993, https://doi.org/10.1016/j.coldregions.2020.102993.
[35] T. Kozlowski, A semi-empirical model for phase composition of water in clay-water systems, Cold Reg. Sci. Technol. 49 (2007) 226–236, https://doi.org/10.1016/j.coldregions.2007.03.013.
[36] J.M. McKenzie, C.I. Voss, D.I. Siegel, Groundwater flow with energy transport and water-ice phase change: numerical simulations, benchmarks, and application to freezing in peat bogs, Adv. Water Resour. 30 (2007) 966–983, https://doi.org/10.1016/j.advwatres.2006.08.008.
[37] M. Zhang, X. Zhang, J. Lu, W. Pei, C. Wang, Analysis of volumetric unfrozen water contents in freezing soils, Exp. Heat Tran. 32 (2019) 426–438, https://doi.org/10.1080/08916152.2018.1535528.
[38] R.W.R. Koopmans, R.D. Miller, Soil freezing and soil water characteristic curves, Soil Sci. Soc. Am. J. 30 (1966) 680–685.
[39] E.J.A. Spaans, J.M. Baker, The soil freezing characteristic: its measurement and similarity to the soil moisture characteristic, Soil Sci. Soc. Am. J. 60 (1996) 13–19.
[40] C. Zhang, Z. Liu, Freezing of water confined in porous materials: role of adsorption and unfreezable threshold, Acta Geotech 13 (2018) 1203–1213.
[41] B.L. Kurylyk, K. Watanabe, The mathematical representation of freezing and thawing processes in variably-saturated, non-deformable soils, Adv. Water Resour. 60 (2013) 160–177.
[42] Z. Liu, X. Yu, Physically based equation for phase composition curve of frozen soils, Transport. Res. Rec. 2349 (2013) 93–99.
[43] J. Teng, J. Kou, X. Yan, S. Zhang, D. Sheng, Parameterization of soil freezing characteristic curve for unsaturated soils, Cold Reg. Sci. Technol. 170 (2020), 102928, https://doi.org/10.1016/j.coldregions.2019.102928.
[44] J. Ren, S.K. Vanapalli, Comparison of soil-freezing and soil-water characteristic curves of two Canadian soils, Vadose Zone J. 18 (2019) 1–14, https://doi.org/10.2136/vzj2018.10.0185.
[45] T. Ma, C. Wei, X. Xia, J. Zhou, P. Chen, Soil freezing and soil water retention characteristics: connection and solute effects, J. Perform. Constr. Facil. 31 (2017), https://doi.org/10.1061/(asce)cf.1943-5509.0000851.
[46] T.F. Azmatch, D.C. Sego, L.U. Arenson, K.W. Biggar, Using soil freezing characteristic curve to estimate the hydraulic conductivity function of partially frozen soils, Cold Reg. Sci. Technol. (2012) 83–84, https://doi.org/10.1016/j.coldregions.2012.07.002, 103-109.
[47] P.J. Williams, The nature of freezing soil and its field behaviour, Nor. Geotech. Inst. (1967) 91–119.
[48] C. Wang, Y. Lai, M. Zhang, Estimating soil freezing characteristic curve based on pore-size distribution, Appl. Therm. Eng. 124 (2017) 1049–1060, https://doi.org/10.1016/j.applthermaleng.2017.06.006.
[49] K. Liang, Experimental Study on the Quantitative Relationship between Frozen Water Content and Specific Surface Area, Beijing University of Civil Engineering and Architecture, 2021.
[50] Y. Chen, Z. Zhou, J. Wang, Y. Zhao, Z. Dou, Quantification and division of unfrozen water content during the freezing process and the influence of soil properties by low-field nuclear magnetic resonance, J. Hydrol. 602 (2021), 126719.
[51] X. Yang, J. Sun, R. Pang, W. Meng, Z. Tao, Experimental study on the variation of unfrozen water content and pore water in unsaturated soil during thawing process, in: IOP Conf. Ser. Earth Environ. Sci, IOP Publishing, 2021, 52111.
[52] F. Jaeger, A. Shchegolikhina, H. Van As, G.E. Schaumann, Proton NMR relaxometry as a useful tool to evaluate swelling processes in peat soils, Open Magn. Reson. J. 3 (2010) 27–45.
[53] T.F.J.A.R. Tice, J.L. Oliphant, Yuanlin Zhu, Y. Nakano, Relationship between the ice and unfrozen water phases in frozen soils as determined by pulsed nuclear resonance and physical desorption data, J. Glaciol. Geocryol. 5 (1983) 37–46.
[54] N.N. Smirnov, V.F. Nikitin, L.I. Stamov, V.V. Tyurenkova, M.N. Smirnova, Modelling of thin wall perforation limit in debris particles impact on space structures, Acta Astronaut. (2022), https://doi.org/10.1016/j.actaastro.2022.09.026. In press.
[55] H. Zhai, Y.J. Dai, J.Y. Wu, R.Z. Wang, L.Y. Zhang, Experimental investigation and analysis on a concentrating solar collector using linear Fresnel lens, Energy Convers. Manag. 51 (2010) 48–55.
[56] K.-J. Dunn, D.J. Bergman, G.A. LaTorraca, Nuclear Magnetic Resonance: Petrophysical and Logging Applications, Elsevier, 2002.
[57] C.H. Sondergeld, R.J. Ambrose, C.S. Rai, J. Moncrieff, Micro-structural studies of gas shales, SPE Unconv. Gas Conf. (2010), https://doi.org/10.2118/131771-MS. SPE-131771-MS.
[58] K. Watanabe, M. Mizoguchi, Amount of unfrozen water in frozen porous media saturated with solution, Cold Reg. Sci. Technol. 34 (2002) 103–110.
[59] S. Hamamoto, P. Moldrup, K. Kawamoto, L. Wollesen de Jonge, P. Schjønning, T. Komatsu, Two-region extended archie's law model for soil air permeability and gas diffusivity, Soil Sci. Soc. Am. J. 75 (2011) 795–806, https://doi.org/10.2136/sssaj2010.0207.
[60] T. Sakaki, M. Komatsu, M. Takahashi, Rules-of-Thumb for predicting air-entry value of disturbed sands from particle size, Soil Sci. Soc. Am. J. 78 (2014) 454–464, https://doi.org/10.2136/sssaj2013.06.0237n.
[61] L. Tang, K. Wang, L. Jin, G. Yang, H. Jia, A. Taoum, A resistivity model for testing unfrozen water content of frozen soil, Cold Reg. Sci. Technol. 153 (2018) 55–63.